Modeling Diatom Frustules as Photonic Crystals

An Honors Thesis submitted in partial fulfillment of the requirements of Honors Studies in Physics

By

Jonathan H. Mishler

2015

Physics
J. William Fulbright College of Arts and Sciences
The University of Arkansas

TABLE OF CONTENTS

FIGURES

ACKNOWLEDGMENTS

I would like to acknowledge Dr. Joseph Herzog for his invaluable mentoring and support through this project. I would also like to thank Dr. Andrew Alverson for his contributions to our understanding of diatoms, and Dr. Keith Roper for the inspiration of this project. Furthermore, I would like to thank Saeed Sarollahi, for his contributions towards some of the COMSOL models used.

I would like to thank Dr. Joseph Herzog, Dr. Andrew Alverson, Dr. William Oliver, and Shawn Irish for serving as members of my committee.

In addition, I would like to thank the Arkansas Department of Higher Education Student Undergraduate Research Fellowship, as well as the University of Arkansas Honors College for their support of this project. I would also like to thank SPIE for their Newport Research Excellence Award.

CHAPTER 1:

INTRODUCTION

1.1 Diatoms

Diatom algae are extremely diverse, unicellular, photosynthetic microorganisms found in marine, freshwater, and brackish habitats [1, 2]. Diatoms are commonly known for their beautiful silica cell walls, called frustules, shown in figure 1.1. Frustules exhibit a unique periodic nano-patterning, distinguishing them from other types of phytoplankton [1, 2]. In the last decade, the optical properties of diatoms have been researched due to their resemblance of photonic crystals [3].

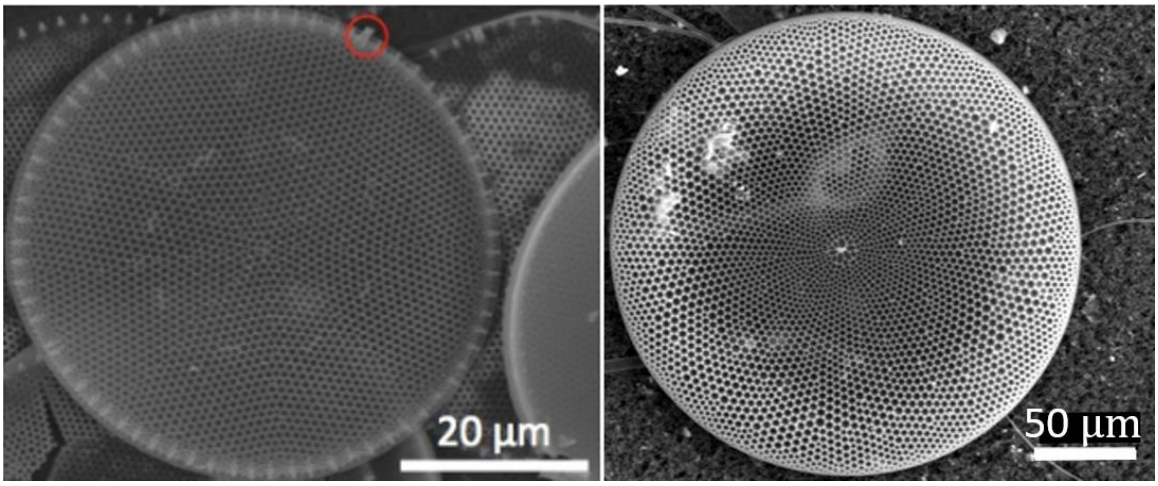

Figure 1.1: (A) SEM image of the centric diatom, *Thalassiosira anguste lineata*. Circled, is the labiate process. This is a single fixed point of asymmetry on the diatom frustule. It is a useful point of reference when considering symmetries present in frustule. (B) SEM image of the centric diatom, *Coscinodiscus Wailesii* [4].

1.2 Photonic Crystals

A crystal is a periodic structure, and a photonic crystal is a periodic structure with periodicity on the order of magnitude of the wavelength of light. They have periodically patterned dielectric nanostructures that can direct the motion of light belonging to certain

electromagnetic frequency bandwidths due to interference effects. The dielectric material and periodicity of the nanostructure determines which bands of light can pass through the material and which are directed around the photonic crystal. Applications of photonic crystals include thin-film optics [5], photonic-crystal fibers [6], photon-state squeezing [7], micro-fabricated lasers [8], and optical computers [9]. As fabrication techniques advance, the number of applications exploiting photonic crystals will grow.

Diatoms, which have geometric structure similar to photonic crystals, are not only considered for their applications as photonic crystals, but also for their use as biomimetic templates for artificially fabricated photonic crystals [10].

A simplified example of a 1D photonic crystal is shown in figure 1.2. This example illustrates what happens in only one layer of a 1D photonic crystal. The layer of dielectric thin film has a thickness of $\lambda/(4n)$, where λ is the wavelength of the incident light corresponding to the central wavelength of the bandgap, and n is the refractive index of the film, are deposited onto a substrate. As the light hits the film, some of it reflects and some transmits into the film, after which the light reflects at the film-substrate interface. Wavelengths centered around λ destructively interfere as they reflect from the films, and constructively interfere when they transmit through the film. This is because the optical path difference of one round trip in the film is equal to half of the wavelength. The two reflected waves are out of phase by half of a wavelength and therefore destructively interfere, while all other wavelengths travel through. Adding more quarter-wavelength dielectric layer increases the number of reflected waves and maximizes the destructive interference. This creates a 1D pattern of dielectric material and is known as a 1D photonic

crystal. The physics behind 1D photonic crystals can be generalized to 2D and 3D photonic crystals.

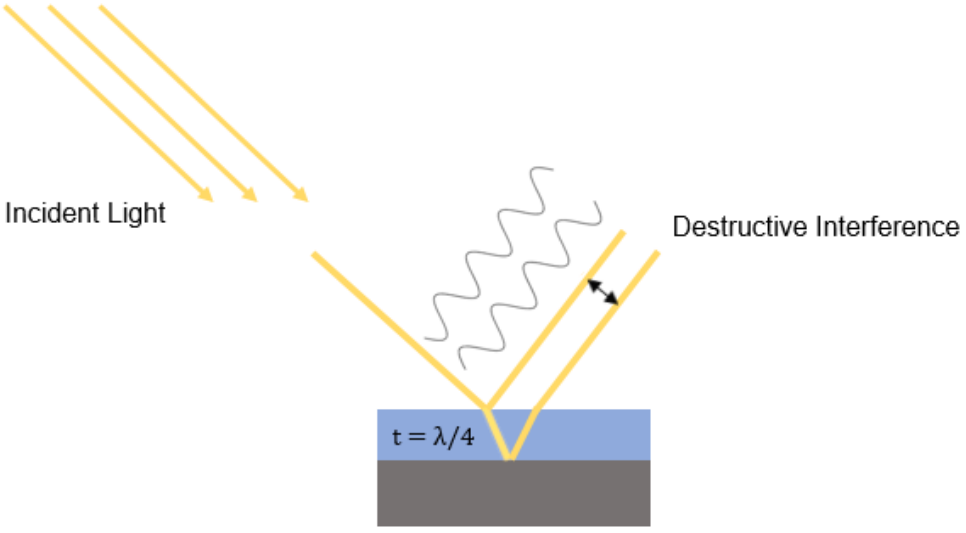

Figure 1.2: Simplified diagram explaining physics behind photonic crystal. Incident light is reflected off of a layering of thin films with thickness λ/4n. Wavelengths of light near λ destructively interfere, allowing only certain wavelengths of light to penetrate the photonic crystal.

To illustrate the band of frequencies that can transmit through a photonic crystal, figure 1.3 shows a typical transmission spectra of photonic crystal. As previously mentioned, wavelengths centered about λ are reflected and destructively interfere. This means that these wavelengths have zero transmission through the photonic crystal. In this figure, a 2D photonic crystal with a hexagonal array of air pores is shown. As seen, the photonic bandgap is a band in the electromagnetic spectrum of which there is zero transmission through the photonic crystal.

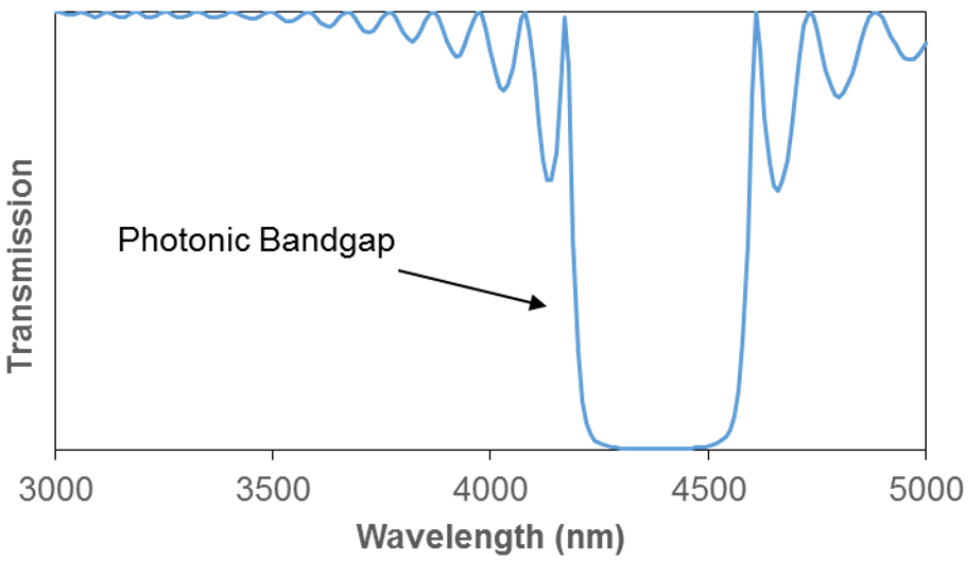

Figure 1.3. Photonic bandgap of 2D model. In the model, the silica slab with air pores is infinitely periodic along the x-axis and approximated to be infinitely periodic along the y-axis by using a large number of periods. The photonic bandgap is the region of the electromagnetic spectrum such that there is zero transmission through the photonic crystal.

CHAPTER 2:

PORE SHAPE CHARACTERIZATION

2.1 Analytical Methods of Geometrical characterization

The diatom lineage dates to roughly 200 million years ago [11], allowing ample time for evolution to refine their physical characteristics and select for different optical properties. To understand how the diatom pore structure influenced their optical properties, diatom pore characterization code was developed with MATLAB. This computational method was built upon existing code developed for other purposes [12]. By understanding this correlation, diatoms can potentially serve as biomimetic templates for artificially developed photonic crystals with desirable optical properties.

This work characterized a single diatom frustule of the marine diatom, *Thalassiosira anguste-lineata*, shown in figure 2.1A. A single diatom pore from figure 2.1B illustrates how the characterization works. To begin, the image file converted into a matrix containing the image data. The length of the scale bar and the number of pixels contained within the scale bar are also input into the function to convert from pixel length to physical length. Using this matrix, the image is converted into a binary image, as shown in Figure 2.1C. The analysis then determines the perimeter, centroid, coordinates, and area of the pore using built-in functions. The program then calculates the radius of a circle whose area is equivalent to the area of the pore using the formula,

$$\boldsymbol{r} = \sqrt{\frac{\boldsymbol{A}}{\boldsymbol{\pi}}}$$

where *A* is the area of the pore, similar to the algorithm in [12]. Here *r* is called the effective radius of the pore. Next, as illustrated in Figure 2.1D, the difference between the radius of the pore and the radius of the circle (Δr) is computed as a function of the angle. The data is then filtered using a Savitsky–Golay filter [13]. The data is normalized relative to the effective radius and plotted in Cartesian coordinates, as illustrated in Figure 2.1E.

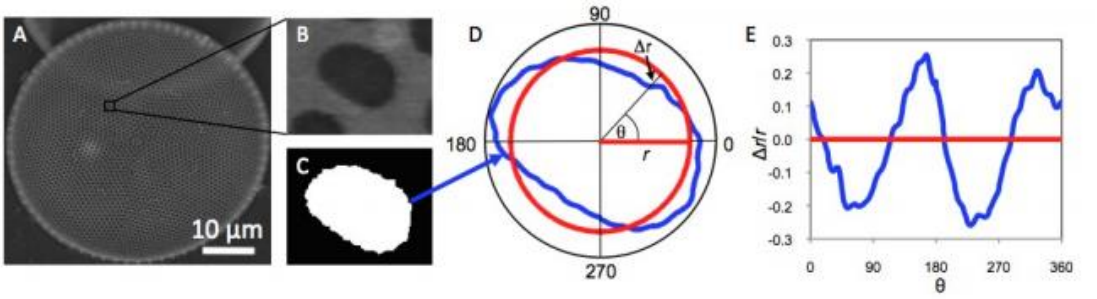

Figure 2.1 [14]: (A) SEM of diatom species *Thalassiosira anguste-lineata*. (B) Single diatom pore. (C) Binary image of single diatom pore. (D) Polar plot of perimeter of diatom pore relative to a circle with an equivalent area. (E) Normalized Cartesian plot of Δr vs. θ.

2.2 Characterizing a Single Diatom

As seen in Figure 2.1A, the diatom is resting on another diatom. This can potentially skew the image and make the pores appear to be more elliptical than they are. Additionally, high-resolution SEM images scans can be slow and can sometimes skew images due to slight drifting of the sample stage during the image photo acquisition. To compensate for both of these, the image was vertically stretched to make the diatom circular. Since the diatom images are relatively small and the program works with pixels, the image was also symmetrically enlarged by a factor of 10 to minimize error.

Pores from the stretched and scaled image were analyzed by the program, which calculated the effective radius, centroid, coordinates, and area of each pore. Figure 2.2A shows a histogram of the effective radii of the pores, which had an average effective radius

of approximately 331 nm. As there are hundreds to thousands of pores on the diatom surface, simply plotting Δr vs. θ for each pore on the same plot is not an effective way to represent the data since it is impossible to determine regions of higher point density. Instead, a pseudocolor plot shown in Figure 2.2B was used to show the superposition of plots of Δr vs. θ. In this plot, the brighter regions indicate a higher point density. To create this plot, the program first partitions θ into bins with a size of 1 degree. The program then counts the number of points of Δr contained in each bin. Next, for each bin of θ, the program partitions Δr into bins. The number of points contained within these bins is then calculated, and the bin matrix is plotted as a pseudocolor plot. This plot is essentially a 2D histogram: a collection of 1D histograms of Δr for each bin of θ.

A 1D histogram of Δr integrated over all angles was created and is shown in Figure 2.2C. This histogram reveals that most values of Δr are close to 0 nm, as expected, and the standard deviation of Δr of the pores is approximately 16.6 nm.

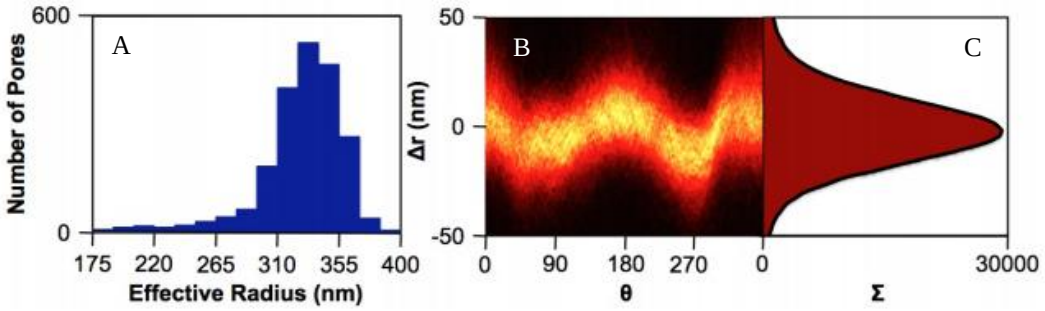

Figure 2.2 [14]: (A) Histogram of effective radii of pores from diatom of Figure 1.1A. (B) 2D Histogram pseudocolor plot of superimposed plots of Δr vs. θ for each diatom pore. Brighter regions indicate higher point density. (C) Histogram of Δr integrated over θ. The black line is a Gaussian fit that determined the standard deviation of Δr to be approximately 16.6 nm.

Observe that in Figure 1.1A, the blue lines highlight the eight sectors of the diatom, each of which have similar areas. To reveal any pore symmetries present in the diatom, the sectors were separated from each other and analyzed individually by the program. These

are presented in Figure 2.3, and the Δr 2D histogram as a function of θ has been created for each sector. The plot revealed several interesting symmetries. First, observe the symmetry between the first four sectors to the left of the labiate process (sectors I – IV), and the first four sectors to the right of the labiate process (sectors V – VIII). The pseudocolor plots of sectors I - IV appear to be continued by the pseudocolor plots of their sectors symmetric to the labiate process. Also notice that there are four sectors in which the Δr values are generally constant as a function of θ, whereas the other four sectors resemble cosine curves. It is interesting to point out that the sectors seem to exist in alternating pairs, where each pair has pores whose Δr values are either constant or resemble cosine curves. For instance, going clockwise, sectors I and V are a pair with pores whose Δr values are constant, while sectors VI and VII are a pair with pores whose Δr values resemble cosine curves. As shown, the pairs continue to alternate for the remainder of the sectors. However, it is important to mention that without examining other images of diatoms, drawing conclusions is problematic. Keeping this in mind, these patterns suggest a potentially important relationship.

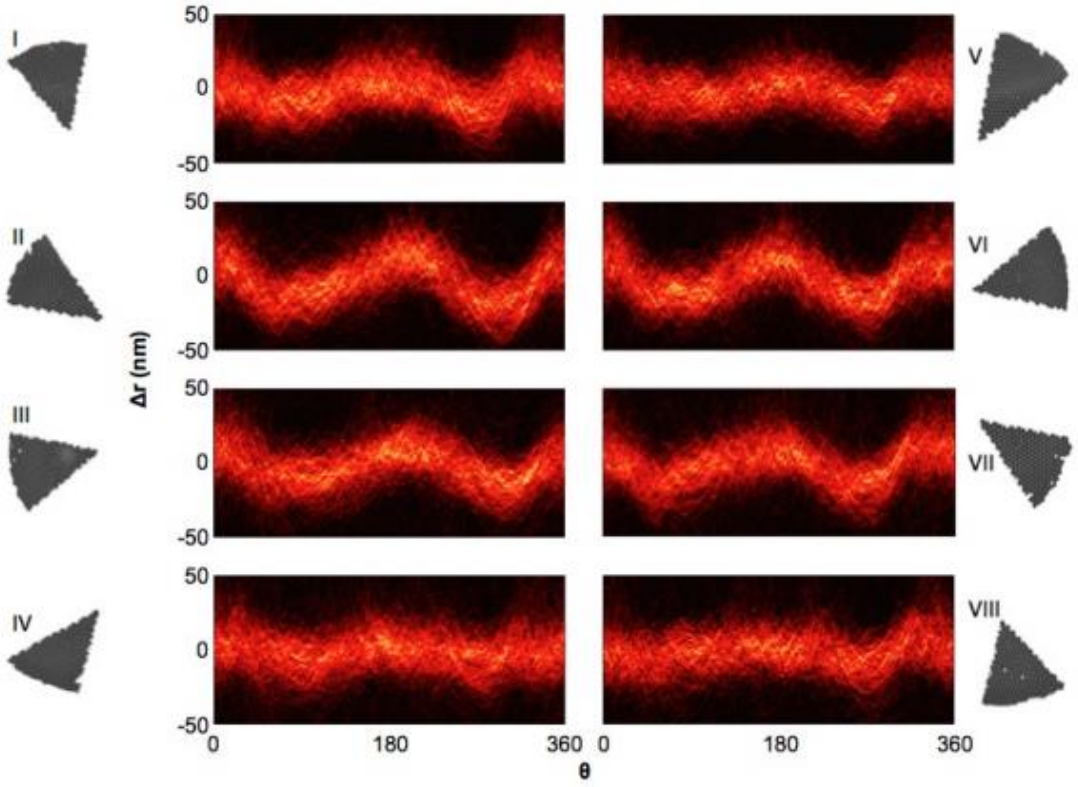

Figure 2.3 [14]: (I – VIII) Pseudocolor plots of superimposed plots of Δr vs. θ for each diatom pore by each diatom sector. Brighter regions indicate higher point density.

At a glance, the diatom pores of *Thalassiosira anguste-lineata* appear to have slightly elliptical shapes. The degree of ellipticity appears to be dependent on the location of the pores. On average, most values of Δr are concentrated between approximately –20 and 20 nm with a greater density at approximately 0 nm, which is consistent with the standard deviation of 16.6 nm.

More diatom samples need to be investigate in order to make any generalization about diatom and pore geometrical relationships. Meanwhile, optical properties of this particular diatom were investigated.

CHAPTER 3:

FINITE ELEMENT METHOD

3.1 Reconstructing the Diatom Frustule

The finite element method is a numerical technique used for solving partial differential equations given a set of boundary conditions [15, 16]. In this approach, the model domain is divided into several elements, which are known as finite elements. The partial differential equations are solved in each element, which closely approximates the entire solution.

To model the optical properties of a diatom frustule, the average physical dimensions of the diatom *Coscinodiscus Sp.* were found from [17], and used to recreate a unit cell of the 3D model. It should be noted that despite the model being 3D, the photonic crystal created was only periodic in two directions, making it a 2D photonic crystal. Figure 3.1 shows the layering of the 3D model, based off of the *Coscinodiscus Sp.* frustule shown on the left. However, the diatom in the SEM image in figure 3.1 is flipped upside down, so the 3D model was adjusted accordingly. Starting from the bottom, there is a periodic silica slab with air pores of radius 342 nm, the thickness of which is approximately 100 nm. The next layer is made up of a periodic array of hexagons with a thickness of over 2 μm. Finally, the upper layer is a silica slab with pores of radius 360 nm, whose material composition is a hybrid of air and silica. As seen in the SEM image, the top layer should be composed of a silica slab with small pores. To reduce computational complexity, the small pores were modeled as one single pore with an effective refractive index as in [17]. Lastly, to the right of figure 3.1, a unit cell of the model is shown, with a period of 1840 nm.

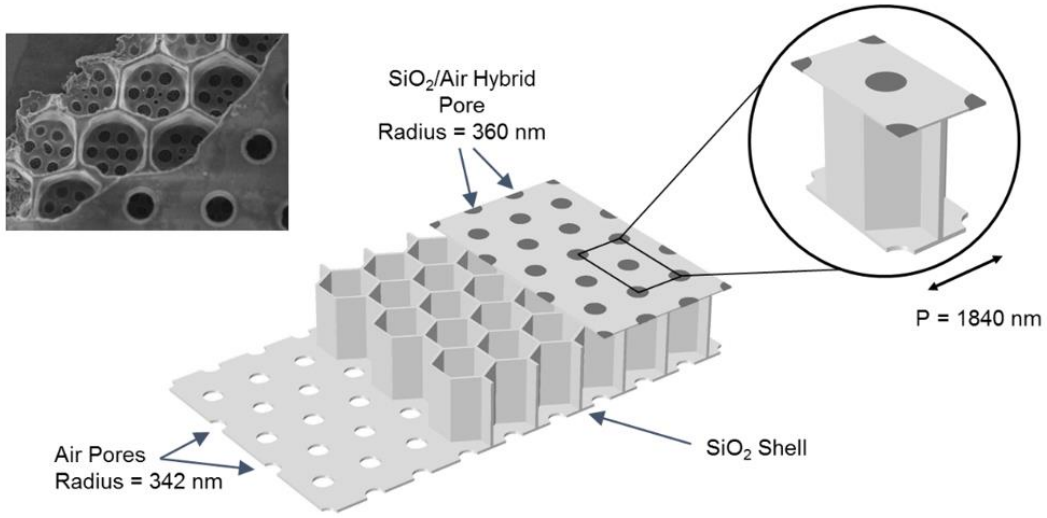

Figure 3.1: COMSOL model of diatom frustule derived from the physical dimensions of a *Coscinodiscus Sp.* diatom. Diatom in SEM image shown on left is flipped upside down, so model was adjusted accordingly. There are three layers in the model, with a unit cell shown on the right.

3.2 3D Model Results

Light between 400 and 700 nm with normal incidence illuminated the photonic crystal, and the transmission spectrum was calculated and is plotted in figure 3.2. This spectrum was initially troubling, as it appears to be a noisy spectrum with no significance. On the right of figure 3.2, the electric field distribution along the given model cross section is shown for wavelengths of 700 and 1000 nm. To locate the source of noise, the model was broken up into four components, where the transmission of each was calculated.

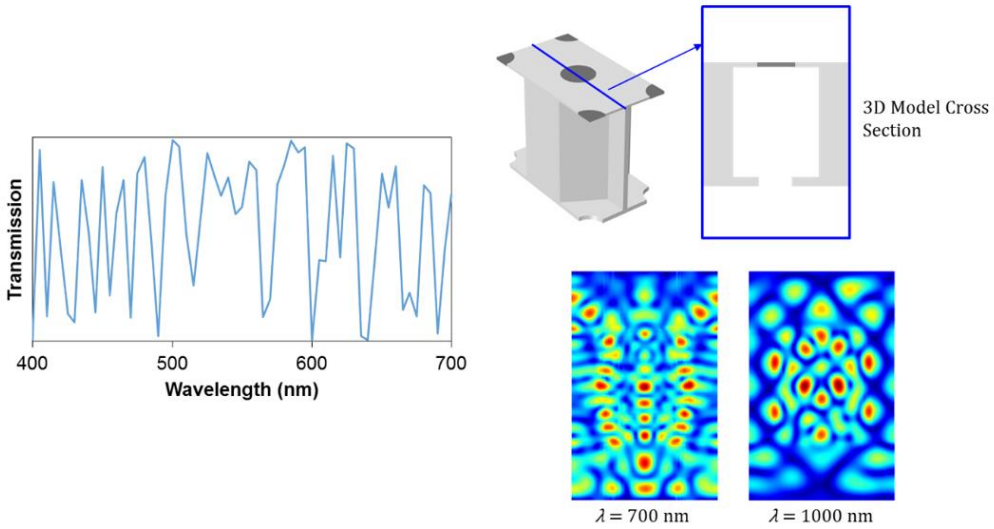

Figure 3.2: On the left is the transmission of light with normal incidence to the three layers of the photonic crystal. On the right is the electric field distribution for a wavelength of 700 and 1000 nm along the given cross section.

Figure 3.3 shows the various sub-models and their corresponding transmission spectra. One thing to note is that the top layer is itself divided into two sub-models, one with air pores, and the other with the silica/air hybrid pores, in order to determine the effects of the hybrid pores.

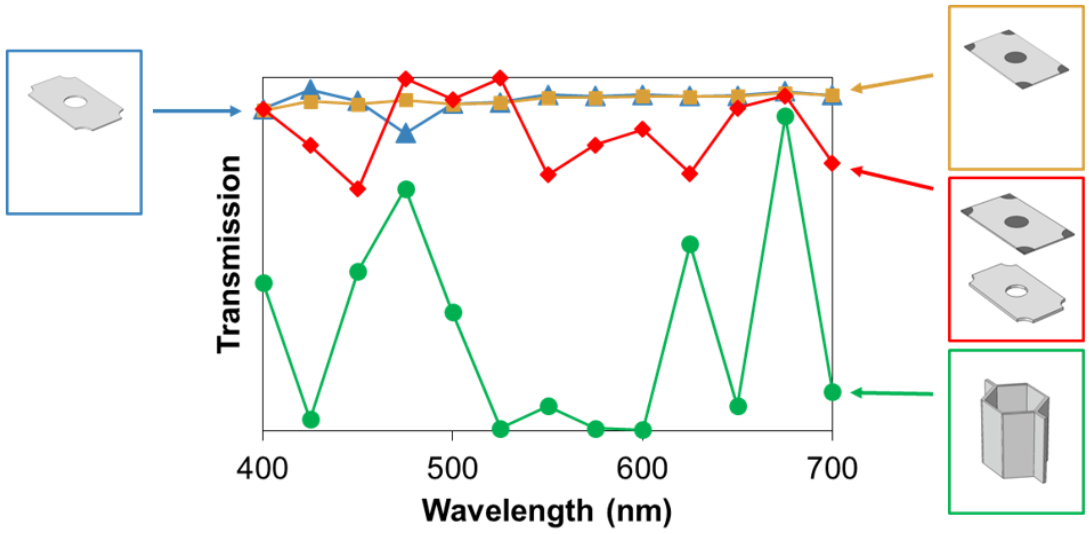

Figure 3.3: The two top layers modelled in orange and blue have an almost identical transmission curve. The top and bottom layers together have an almost perfect transmission, however the hexagonal model is significantly noisier.

As shown in blue and orange, the two top layers with the air and hybrid pores have almost identical, perfect transmissions. The combined top and bottom layer model has slightly less transmission, but still almost perfect. However, the hexagonal layer has a much more fluctuating transmission, indication that it is likely the source of noise. To further investigate the 2D properties of these structures, 2D optical models were created.

3.3 2D Model Results

The 2D model was designed as shown in figure 3.4. This module is a rectangle with periodic boundary conditions on the left and right sides. This is modeled as being infinitely periodic along the x-axis. The model has a finite number of periods in the y-direction and is flexible to study the effects of a finite number of periods. In particular, figure 3.4 has 7 periods. The direction into the plane (z) is modeled to be infinitely long. The Transmission of light through the model was calculated as a function of both wavelength and period. The results of these computations are shown in figure 3.5.

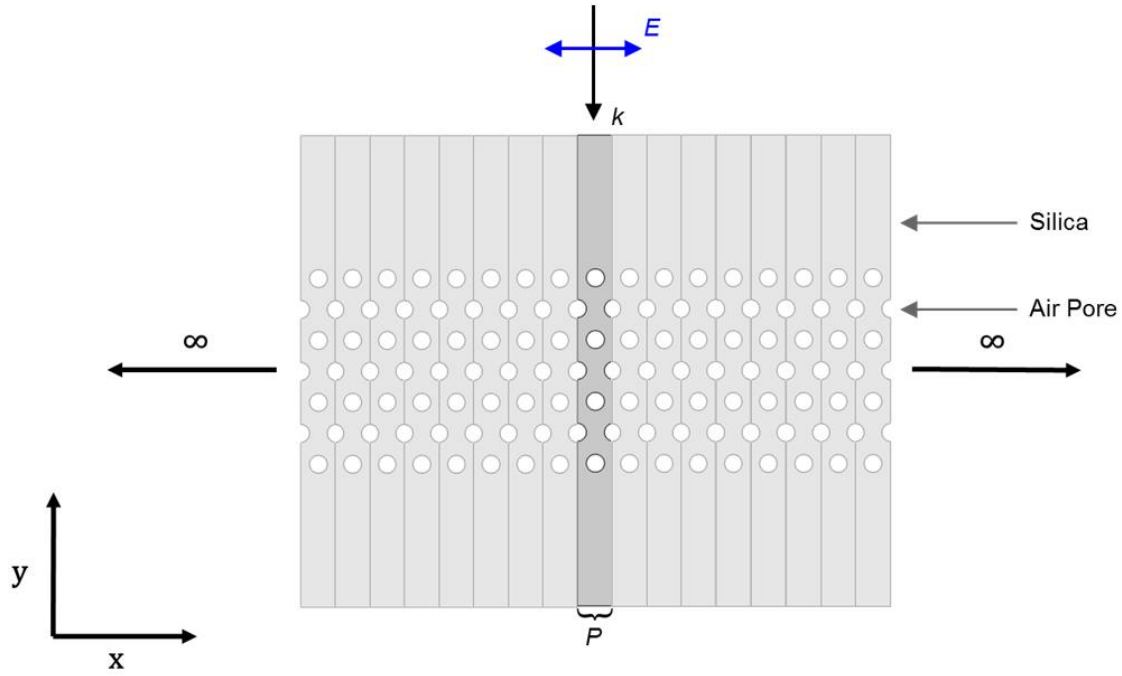

Figure 3.4: 2D model of photonic crystal. The model is infinitely periodic along the x-axis, and quasi-periodic along the y-axis. The outer shell is made of silica, and the pores are made of air. The k-vector is perpendicular to the infinite periodicity of the model, whereas the electric field is parallel (TM) to the infinite periodicity of the model.

As seen in figure 3.5, the central wavelength the photonic band gap shifts towards the infrared and widens as the period increase. Plotting the central wavelength in the photonic band gap as a function of period reveals a linear relationship between the two. Also, as seen in figure 3.5, as the period increases from 200 nm, a noisy transmission spectrum in introduced into the optical region, explaining why the transmission through the 3D model was noisy.

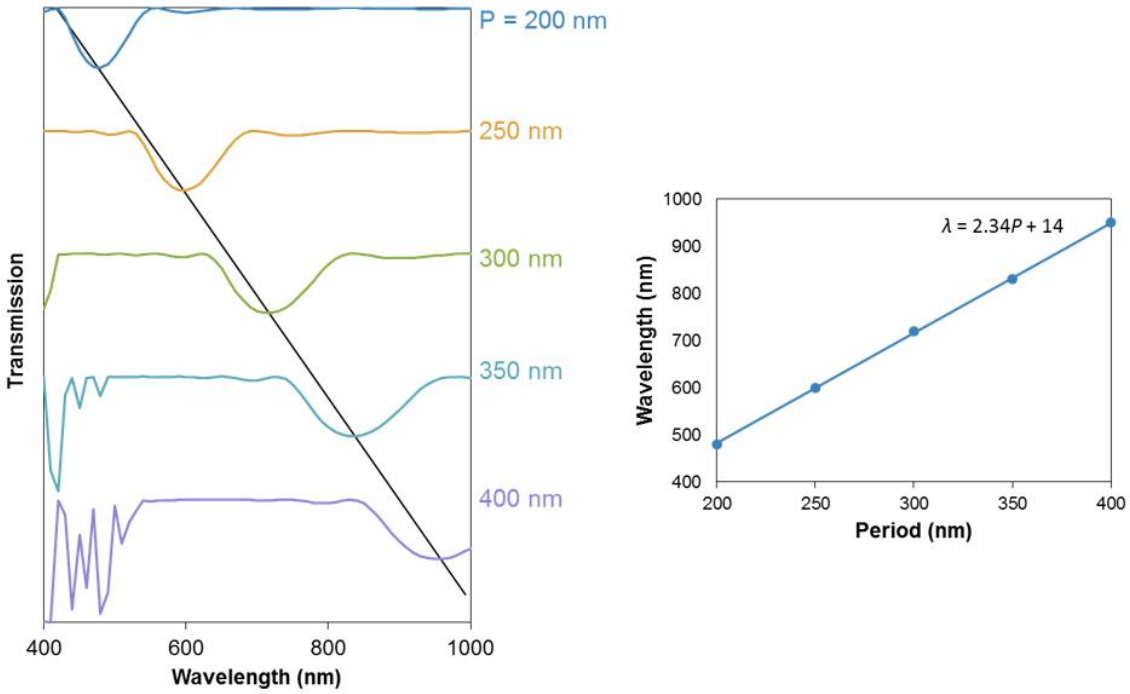

Figure 3.5: Waterfall plot of transmission as a function of wavelength with varying periods. As the period increases, the photonic bandgap shifts towards the infrared and widens, introducing noise into the visible band. Using the linear relationship between period and central photonic band wavelength, it is possible to predict the location of the photonic band gap of the 2D photonic crystal for any period. The radius of the pores is P/4 in each of the models, which is close to the radius in the 3D model.

Extrapolating the linear relationship between period and central wavelength of the bandgap, the location of the bandgap of the photonic crystal with a period of 1840 nm was estimated to be centered about 4319.6 nm. When modelling the 2D photonic crystal with a period of 1840 nm, the photonic bandgap is found to be centered about 4390 nm, which is close to the predicted wavelength, as shown in figure 3.6. These results indicate that in the 3D model, a noisy spectrum is expected in the visible range, and the transmission curve should be restricted to the far infrared.

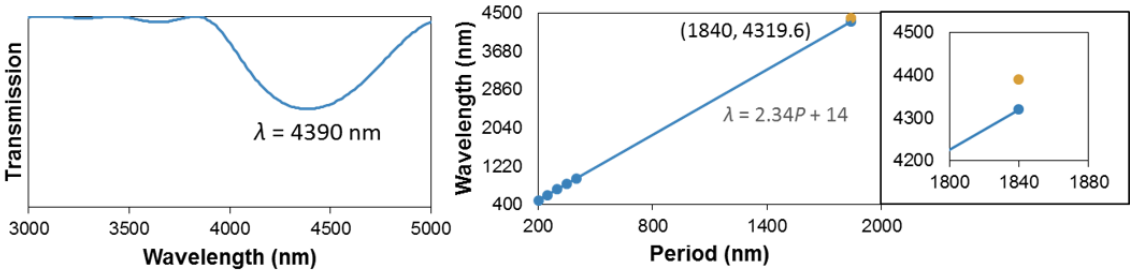

Figure 3.6: Modelling the photonic bandgap for a 2D photonic crystal with period 1840 nm. The expected bandgap centered about 4319.6 nm is close to the bandgap found at 4390 nm.

Next, each of the diatom's three layers were modeled in 2D. However, to more closely approximate the several periods found in diatoms, 15 periods were used instead of 7, the results of which are shown in figure 3.7. To the right of each transmission curve is an enlarged unit cell of each photonic crystal.

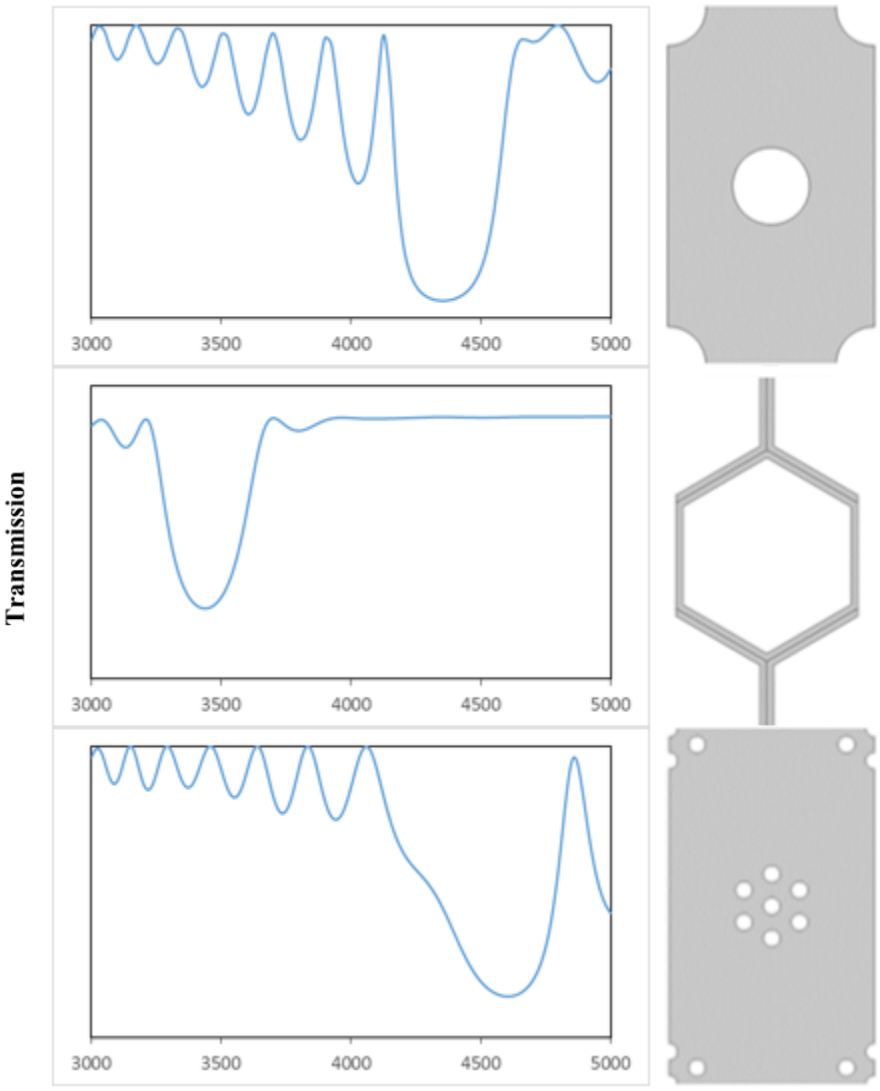

Figure 3.7: Modelling each of the layers of the diatom shown in figure 3.1 in 2D gives the following transmission curves. To the right of each transmission curve is an enlarged unit cell of the photonic crystal.

CHAPTER 4:

CONCLUSION

Diatoms possess several unique characteristics that likely influence their optical properties. Diatoms not only have elliptical pore geometries, but also many layers of periodic patters with varying thicknesses and periodicities. In the 2D model, a linear relationship between period and location of the photonic bandgap was found, indicating that the relevant optical properties for diatoms may be confined to the far infrared. Future work includes the continuation of 2D models, where each layers of the diatom can be modeled. In addition to the 2D models, new 3D models, including a radially symmetric 3D model will be created to study the effects of the diatom radial symmetry.

APPENDIX A

USING COMSOL

After defining the relevant physical and electromagnetic parameters, the geometry was created. Material properties, most notably refractive index, were found from http://refractiveindex.info/, and processed with Microsoft Excel. The material properties were then interpolated by a function generated by COMSOL. Floquet periodic boundary conditions were applied along the x-axis, and y-axis when appropriate. Ports were placed along the top and bottom of the model, and the polarization of the plane wave was defined. Scattering boundary conditions and perfectly matched layers, which absorbed unwanted light were used where appropriate. After meshing the model with a free tetrahedral mesh, and the perfectly matched layers with a swept mesh, the model was computed with the wavelength of light being parametrically swept.

APPENDIX B

USING THE SUPERCOMPUTER CLUSTERS

Some of the models were computed with the supercomputer clusters at the HPCC. After receiving access to the clusters, the following steps were taken to use the clusters:

1. SSH into razor.uark.edu

2. Connect to a compute node using the following command:

“qsub -I -l nodes=1:ppn=12 -q mem96GB12core -l walltime=3:00:00:00”

where nodes represents the number of nodes desired, ppn is the number of processors used per node, -q “ “ is the name of the node being connected to, and walltime is the amount of time the node is being reserved for.

3. After connecting to the node, "/share/apps/bin/vnc-display-windows.sh" was typed into the SSH secure shell. The following messages were then displayed on the shell:

“LOCALNODE > plink.exe -L ####:compute####:#### youruarkid@stargate.uark.edu”

“LOCALNODE > vncviewer :##”

4. “plink.exe -L ####:compute####:#### youruarkid@stargate.uark.edu” was then copied and pasted into the command prompt.

5. Tightvnc was then opened and “localhost:##” was entered into the connection window. The “##” are the two numbers found in step 3.

6. A command prompt was opened in tightvnc, where

“sort -u $PBS_NODEFILE >hostfile” was then copied and pasted into the command prompt. This command puts the names of the nodes into a textfile which tells COMSOL which nodes to connect to.

7. “COMSOL /LicensePath” was typed into the command prompt, which opened COMSOL with the specified license.

8. The COMSOL model was opened, and the COMSOL cluster settings were used.

BIBLIOGRAPHY

[1] Grethe R. Hasle; Erik E. Syvertsen; Karen A. Steidinger, Karl Tangen (1996-01-25). "Marine Diatoms". In Carmelo R. Tomas. *Identifying Marine Diatoms and Dinoflagellates*. Academic Press. pp. 5–385.

[2] Frank Eric Round; R. M. Crawford; D. G. Mann (1990). "The Diatoms: Biology & Morphology of the Genera". Cambridge University Press.

[3] Fuhrmann, T., Landwehr, S., El Rharbi-Kucki, M. and Sumper, M., "Diatoms as living photonic crystals", Applied Physics B: Lasers and Optics 78, 257-260 (2004).

[4] Universidad de Colima. Elaborada por Fis. Darío Pozas Zepeda
Visitante No. 4528 desde 07/ene/2010 http://fejer.ucol.mx/meb/galeria.php

[5] Bermel, Peter et al., "Improving thin-film crystalline silicon solar cell efficiencies with photonic crystals" Optics Express, Vol. 15, Issue 25, pp. 16986-17000 (2007).

[6] Dudley, John M. et al., "Supercontinuum generation in photonic crystal fiber" Rev. Mod. Phys., Vol.78, Issue 4, pp. 1135-1184 (2006).

[7] M. Banaee and J. Young, "Squeezed state generation in photonic crystal microcavities," Opt. Express 16, 20908-20919 (2008).

[8] Izeikis, V., Matsuo, S., Juodkazis, S. and Misawa, H. (2006) [Femtosecond Laser Microfabrication of Photonic Crystals, in 3D Laser Microfabrication: Principles and Applications] (eds H. Misawa and S. Juodkazis), Wiley-VCH Verlag GmbH & Co. KGaA, Weinheim, FRG.

[9] Ouellette, J., "Seeing the Future in Photonic Crystals," Industrial Physicist, Vol. 7, No. 6, pp. 14-17, 2001.

[10] Hlúbiková, D., A. T. Luís, V. Vaché, L. Ector, L. Hoffmann, and P. Choquet. "Optimization of the Replica Molding Process of PDMS Using Pennate Diatoms." Journal of Micromechanics and Microengineering 22.12: (2012).

[11] Ulf Sorhannus, "A nuclear-encoded small-subunit ribosomal RNA timescale for diatom evolution, Marine Micropaleontology", Volume 65, Issues 1–2, 29 October 2007, Pages 1-12

[12] P. Blake, W. Ahn, and D.K. Roper, “Enhanced uniformity in arrays of electroless plated spherical gold nanoparticles using tin presensitization,” Langmuir

[13] Abraham. Savitzky and M. J. E. Golay. “Smoothing and Differentiation of Data by Simplified Least Squares Procedures”. *Analytical Chemistry* **1964** 36(8), 1627-1639.

[14] Jonathan Mishler, Philip Blake, Andrew J. Alverson, D.K. Roper, Joseph B. Herzog. “Diatom frustule photonic crystal geometric and optical characterization”. *Nanobiosystems: Processing, Characterization, and Applications VII* **2014**.

[15] Hrennikoff, Alexander (1941). "Solution of problems of elasticity by the framework method". *Journal of applied mechanics* **8.4**: 169–175.

[16] Courant, R. (1943). "Variational methods for the solution of problems of equilibrium and vibrations". *Bulletin of the American Mathematical Society* **49**: 1–23.

[17] Anne Kirsti Noren. Characterization of Structure and OPtical Properties of Diatoms for improved Solar Cell Efficiency. Norwegian University of Science and Technology.